

Partial mixing and the formation of ^{13}C pockets in AGB stars: effects on the s -process elements

J. F. Buntain¹, C. L. Doherty^{2,1}, M. Lugaro^{2,1}, J. C. Lattanzio¹, R. J. Stancliffe³ and A. I. Karakas^{1,4}

¹Monash Centre for Astrophysics (MoCA), School of Physics and Astronomy, Monash University, Victoria 3800, Australia

²Konkoly Observatory, Research Centre for Astronomy and Earth Sciences, Hungarian Academy of Sciences, H-1121 Budapest, Hungary

³Argelander Institute for Astronomy, University of Bonn, Auf dem Huegel 71, D-53121 Bonn, Germany

⁴Research School of Astronomy and Astrophysics, Australian National University, Canberra, ACT 2611, Australia.

9 October 2018

ABSTRACT

The production of the elements heavier than iron via *slow* neutron captures (the s process) is a main feature of the contribution of asymptotic giant branch (AGB) stars of low mass ($< 5 M_{\odot}$) to the chemistry of the cosmos. However, our understanding of the main neutron source, the $^{13}\text{C}(\alpha, n)^{16}\text{O}$ reaction, is still incomplete. It is commonly assumed that in AGB stars mixing beyond convective borders drives the formation of ^{13}C *pockets*. However, there is no agreement on the nature of such mixing and free parameters are present. By means of a parametric model we investigate the impact of different mixing functions on the final s -process abundances in low-mass AGB models. Typically, changing the shape of the mixing function or the mass extent of the region affected by the mixing produce the same results. Variations in the relative abundance distribution of the three s -process peaks (Sr, Ba, and Pb) are generally within ± 0.2 dex, similar to the observational error bars. We conclude that other stellar uncertainties - the effect of rotation and of overshoot into the C-O core - play a more important role than the details of the mixing function. The exception is at low metallicity, where the Pb abundance is significantly affected. In relation to the composition observed in stardust SiC grains from AGB stars, the models are relatively close to the data only when assuming the most extreme variation in the mixing profile.

Key words: stars: abundances – stars: AGB and post-AGB – nuclear reactions, nucleosynthesis, abundances

1 INTRODUCTION

Asymptotic giant branch (AGB) stars are a significant site of the origin of chemical matter in the Universe, and in particular of the elements heavier than Fe. The AGB is populated by low- and intermediate-mass stars (in the range ~ 0.5 to $10 M_{\odot}$) evolved past core H and He burning. Their structure is characterised by an inert, degenerate C-O core, a He- and a H-burning shell, separated by a He-rich “intershell”, and an extended, convective, H-rich envelope. The H-burning shell is active most of the time, except when recurrent thermal instabilities of the He shell (thermal pulses, TPs) result in partial He burning and the ^{12}C enrichment of the intershell. Most of the stellar mass is located in the envelope, which is eroded by strong, dusty stellar winds. Recurrent dredge-up episodes (the third dredge-up, TDU) that may follow each TP bring material rich in nuclei freshly synthesized by nuclear reactions, from the intershell to the surface of the

star. From there, the winds carry the enriched matter into the stellar surroundings. Once the winds have removed most of the envelope mass, the star moves onto the post-AGB track, evolving at constant luminosity towards higher temperatures. The C-O core eventually is left as a cooling white dwarf. For detailed reviews on AGB stars see Herwig (2005), Straniero et al. (2006), and Karakas & Lattanzio (2014).

The cosmic abundances of the elements heavier than Fe are predominately produced via the capture of free neutrons because their large number of protons (> 26) results in a strong Coulomb barrier (Burbidge et al. 1957). In the case of the *slow* neutron-capture process (the s process) typical neutron densities are of the order of 10^7 cm^{-3} , at which the timescale of the neutron capture is longer than the timescale of the β decay of unstable isotopes and the nuclear production path proceeds along a chain of stable nuclei. Nuclei with magic numbers of neutrons N along the path, e.g., ^{88}Sr ($N = 50$), ^{138}Ba ($N = 82$), and ^{208}Pb ($N = 126$), have lower

neutron-capture cross sections relative to nearby nuclei and tend to accumulate during the *s* process. This leads to the presence of three peaks in the *s*-process abundance distribution, corresponding to the three magic numbers above. The *s*-process stellar sites are identified with the hydrostatic burning phases of massive stars (Raiteri et al. 1991; Pignatari et al. 2010) and the AGB phase (Iben & Truran 1978; Gallino et al. 1998).

In AGB stars the *s* process occurs in the intershell, both within the convective regions generated by the TPs and during the periods between TPs (the so-called interpulse) in radiative conditions (Straniero et al. 1997; Gallino et al. 1998; Busso et al. 1999; Goriely & Mowlavi 2000; Lugaro et al. 2003a; Cristallo et al. 2009; Bisterzo et al. 2010; Lugaro et al. 2012). In the convective regions the neutron source is the $^{22}\text{Ne}(\alpha, n)^{25}\text{Mg}$ reaction. Nuclei of ^{22}Ne are abundant inside the convective TPs because they are the result of double α captures on the ^{14}N present in the H-burning ashes and ingested by the TP convective zone. Neutrons are released over a relatively short time scale (of the order of years), which results in relatively high neutron densities (approximately, up to 10^{10} cm^{-3} in AGB stars of initial mass $< 4 M_{\odot}$ and to 10^{13} cm^{-3} in AGB stars of higher masses, e.g. van Raai et al. 2012; Fishlock et al. 2014; Straniero et al. 2014). Such neutron densities drive the activation of *branching points* on the *s*-process path, where unstable nuclei with half lives of the order of or larger than a day can capture a neutron instead of decaying, resulting in a branch on the path of neutron captures. However, the ^{22}Ne neutron source requires temperatures above 300 MK to be efficiently activated, which are only found in stellar models of mass above around $3 M_{\odot}$ (Iben & Truran 1978; Abia et al. 2001; van Raai et al. 2012; Karakas et al. 2012).

In the lower-mass AGB stars, which are observed to be strongly *s*-process enriched (e.g., Busso et al. 2001; Abia et al. 2002), the best candidate neutron source is instead the $^{13}\text{C}(\alpha, n)^{16}\text{O}$ reaction, which is activated at 90 MK. Because the amount of ^{13}C produced by H burning is not enough to explain the observed *s*-process enhancements, it is assumed that a partial mixing zone (PMZ) forms at the deepest extent of each TDU episode, where protons from the envelope are mixed into the intershell. The resulting compositional profiles are mostly determined by the relative rates of the proton-capture reactions on ^{12}C and ^{13}C , which are functions of the number of protons, ^{12}C , and ^{13}C . In the region of the PMZ where the ratio of the number of protons to ^{12}C is < 0.5 the $^{12}\text{C}(\text{p}, \gamma)^{13}\text{N}(\beta^+ \nu)^{13}\text{C}$ reaction chain results in a thin region rich in ^{13}C known as the *^{13}C pocket* (Goriely & Mowlavi 2000; Lugaro et al. 2003a). Typically, an extent in mass of the pocket $\sim 10^{-3, -4} M_{\odot}$ is required to match the observations (Gallino et al. 1998). Where the number of protons is > 0.5 further $^{13}\text{C} + \text{p}$ reactions produce a ^{14}N -rich region, which we will refer to as the *^{14}N pocket*.

The ^{13}C nuclei typically burn over long timescales ($\sim 10^4$ yr) during the interpulse periods, which results in a slow burning and low neutron densities, roughly 10^7 cm^{-3} . Because the ^{13}C nuclei are produced from proton captures on mostly primary ^{12}C made by the triple- α reaction, the ^{13}C neutron source is of primary origin, i.e., the number of ^{13}C nuclei is largely independent of the stellar metallicity. The number of Fe seeds is instead metallicity dependent. It fol-

lows that the number of free neutrons available in the ^{13}C pocket increases with decreasing metallicity and that the second and third *s*-process peaks at Ba and Pb are more efficiently produced as the metallicity decreases. This effect explains the origin and evolution of most of the *s*-process elements in our Galaxy (Travaglio et al. 1999, 2001, 2004).

The main problem with the ^{13}C -pocket model is that although many possibilities have been proposed, the main mixing mechanism leading to the formation of the ^{13}C pocket is still unknown (see, e.g., discussion in Busso et al. 1999; Karakas & Lattanzio 2014). The aim of the present paper is to explore a variety of mixing profiles and their impact on *s*-process abundances considering the full evolution along the thermally pulsing AGB phase of six stellar models of masses between 1.25 and $4 M_{\odot}$ ¹ and metallicities 0.02, 0.01, and 0.0001. This exploration will reveal to us if and when significant variations in the final *s*-process abundances occur due to changes in mixing profile leading to the formation of the PMZ. In Sec. 2 we summarise the different scenarios and models for the formation of the ^{13}C pocket currently present in the literature. In Sec. 3 we present our models, in Sec. 4 the results, and Sec. 5 is dedicated to discussion and conclusion.

2 CURRENT MODELS FOR THE FORMATION OF ^{13}C POCKETS

A range of possibilities and models has been proposed so far to mix protons into the He intershell at the deepest extent of each TDU episode, where a sharp discontinuity is present between the H-rich convective envelope and the H-rich radiative interhell. Early on, Hollowell & Iben (1988) showed that in AGB stars of low mass and low metallicity a semi-convective region can form between the H-rich envelope and the C-rich intershell after each TP due to the increased opacity below the convective envelope. More recently, Herwig (2000) and Cristallo et al. (2009) successfully employed convective overshoot to reproduce the mixing mechanism responsible for the PMZ. Herwig (2000) modelled the overshoot via the diffusion coefficient while Cristallo et al. (2009) via the convective velocity, both using an exponential decay function of the form:

$$A \simeq A_0 \exp\left(-\frac{d}{\beta H_p}\right) \quad (1)$$

where A is either the diffusion coefficient or the convective velocity, A_0 its value close to the formal convective boundary (defined by the Schwarzschild criterion), d the distance from the formal convective boundary, H_p the pressure scale height, and β (also named f) the free overshoot parameter that controls the profile of the exponential decay,

¹ We do not consider higher masses because observations of AGB stars indicate that the formation of the ^{13}C pocket does not occur, or that its impact is very marginal, in more massive AGB stars where the ^{22}Ne neutron source is activated instead (García-Hernández et al. 2013). This is in agreement with the results obtained by models that include the PMZ using overshoot (Goriely & Siess 2004; Cristallo et al. 2015).

i.e., the region affected by the mixing and the extent of the final ^{13}C pocket.

Cristallo et al. (2009, 2011, 2015) presented and discussed detailed *s*-process models and results based on this scheme (the FRUITY database, <http://fruity.oa-teramo.inaf.it/>). The results are very similar to those obtained using the parametric model that we present below, where the PMZ is introduced artificially using an exponential mixing profile (for a detailed comparison between the two sets of models see Lugaro et al. 2012; Fishlock et al. 2014; Karakas & Lugaro 2016).

The main difference between Herwig (2000) and Cristallo et al. (2009) is that Cristallo et al. (2009) only apply the overshoot to the base of the convective envelope during the TDU, while Herwig (2000) applies it to all convective boundaries, including those of the TPs. This results in the dredge-up of C and O from the core into the intershell with crucial implications on the formation of the ^{13}C pocket and the final *s*-process results (Lugaro et al. 2003a). In fact, a higher amount of ^{12}C in the intershell leads to a higher abundance of ^{13}C , and subsequently a higher number of free neutrons. Full *s*-process models including this effect have been developed by Pignatari et al. (2016) and Battino et al. (2016).

Internal gravity waves caused by convective motions beating on the convective/radiative interface are also suggested by Denissenkov & Tout (2003); Battino et al. (2016) to produce the PMZ and produce PMZ similar to those resulting from the overshoot models.

Another scenario is related to mixing driven by magnetic fields, as discussed in detail by Nucci & Busso (2014) and Trippella et al. (2016). The results from this scenario differs from all the others in that the mixing mechanism is not tied to the convective envelope boundary, with the result that the ^{13}C pocket is more extended in mass and the ^{14}N pocket does not form.

Finally, mixing resulting from stellar rotation produce ^{13}C pockets too small ($\sim 10^{-7} M_{\odot}$) to reproduce the observations (Langer et al. 1999). Furthermore, rotational mixing can be present while the neutrons are released inside ^{13}C and ^{14}N pockets produced, e.g., by overshoot. This mixing can strongly inhibit the *s* process by carrying ^{14}N , which is a neutron poison via the $^{14}\text{N}(n,p)^{14}\text{C}$ reaction (Wallner et al. 2016), from the ^{14}N pocket (and/or the H-burning ashes, if the ^{14}N pocket is absent) into the ^{13}C pocket (Herwig et al. 2003; Siess et al. 2004; Piersanti et al. 2013).

In a number of the current models of the *s* process in AGB stars, a PMZ or a ^{13}C pocket is introduced artificially at the deepest extent of each TDU episode, with its extension and mixing or abundance profile treated as relatively free parameters. The models of Gallino et al. (1998) (and follow-up studies by, e.g., Bisterzo et al. 2010, 2011; Liu et al. 2015) are calculated by including some ^{13}C in the intershell and exploring a large variety of extents and abundance profiles. The models of, e.g., Goriely & Mowlavi (2000); Lugaro et al. (2012); Fishlock et al. (2014); Shingles et al. (2015); Karakas & Lugaro (2016) instead are calculated including a PMZ by means of an artificial mixing profile, driving the mixing of protons that subsequently produce a ^{13}C abundance profile. The mixing is modelled using an exponential function where the exponent is a linear function of

the mass (“standard” case, see details in Sec. 2.1) and different mass extents of the mixing are tested, from about 1/100th to 1/5th of the mass of the intershell.

Goriely & Mowlavi (2000) further analysed the effect of modifying the mixing function to generate proton profiles decreasing with the mass depth faster or slower than the standard case. They found that changing the H profile does not significantly affect the final *s*-process abundance distribution and concluded that these are only marginally dependent on the shape of the H profile, whereas the extent in mass of the mixing and the amount of TDU more significantly affect the surface enrichment. However, the study carried out by Goriely & Mowlavi (2000) was quite limited. The nucleosynthesis was followed in four stellar models of masses between 1.5 and 3 M_{\odot} and metallicities between 0.001 and 0.02 only during one representative interpulse and TP phase, rather than over the whole AGB phase. Potential feedback effects on the nucleosynthesis during the AGB evolution were not considered. Furthermore, given the large variety of possible mixing profiles potentially resulting from the different physical processes for the formation of the PMZ described above, a detailed study dedicated to the impact of such variations on the final *s*-process abundances is required and presented here.

3 STELLAR MODELS

3.1 The stellar structure sequences

We use stellar structure models previously calculated from the zero-age main sequence to the end of the AGB phase using the Monash stellar structure code (Lattanzio 1986) and including mass loss during the AGB phase using the prescription of Vassiliadis & Wood (1993). We considered the 1.5 M_{\odot} $Z = 0.0001$ model from Lugaro et al. (2012), the 3 M_{\odot} and 4 M_{\odot} models of metallicity $Z = 0.02$ from Karakas (2010), the 3 M_{\odot} model of $Z = 0.01$ from Shingles & Karakas (2013), and the 1.25 M_{\odot} and 1.8 M_{\odot} models of metallicity $Z = 0.01$ from Karakas et al. (2010). The inputs used for the structure calculations were the same for all the models, except that the $Z = 0.01$ models were computed with the inclusion of the C- and N-rich low temperature opacity tables from Lederer & Aringer (2009), and that convective overshoot was included in the 1.25 M_{\odot} and 1.8 M_{\odot} models by extending the position of the base of the convective envelope by N_{ov} pressure-scale heights with $N_{\text{ov}} = 4$ and 3, respectively (for more details, see Karakas et al. 2010). This overshoot has the effect of deepening the TDU, but does not lead to the formation of the PMZ in the top layers of the intershell because we use homogeneous mixing in the overshoot region.

The main structural features of the selected models are presented in Table 1 where we report: the initial stellar mass (Mass) and metallicity (Z), the number of thermal pulses (TPs), the number of TDU episodes (TDUs), the total mass dredged-up by the TDU ($M_{\text{dred}}^{\text{tot}}$), the maximum temperature in the TPs ($T_{\text{TP}}^{\text{max}}$), and the final envelope mass ($M_{\text{env}}^{\text{fin}}$). The values of $M_{\text{env}}^{\text{fin}}$ in the case of the $Z = 0.02$ models are still relatively high due to convergence issues at the end of the calculations (Lau et al. 2012). Due to the high mass-loss rate at this point of the evolution, only one or two more TPs

Table 1. Details of the stellar structure models. All the masses are in unit of M_{\odot} and the temperature in MK.

Mass	Z	TPs	TDUs	$M_{\text{dred}}^{\text{tot}}$	$T_{\text{TP}}^{\text{max}}$	$M_{\text{env}}^{\text{fin}}$
1.25	0.01	10	3	0.013	246	0.026
1.8	0.01	12	6	0.041	266	0.014
3	0.01	22	17	0.120	306	0.004
3	0.02	25	16	0.081	302	0.676
4	0.02	17	15	0.056	332	0.958
1.5	0.0001	18	15	0.059	282	0.022

are possible before the envelope is lost and it is uncertain if any more TDUs would occur following these TPs. Hence, we consider the final abundances computed for these models close enough to those that would result from adding an extra one or two TPs.

3.2 The stellar nucleosynthesis sequences

The *s*-process nucleosynthesis was calculated using the Monash post-processing code (Cannon 1993), which takes stellar structure information, such as temperature, density, and convective velocity as a function of interior mass and time, and solves implicitly the set of equations that simultaneously describe the abundance changes due to nuclear reactions and to mixing via a two-stream advective scheme. We assumed scaled-solar initial compositions, taking the solar abundances from the compilation by Asplund et al. (2009). We include the PMZ artificially in the post-processing phase by forcing the code to mix a small amount of protons from the envelope into the intershell at the end of each TDU. The method is described in detail in the following section. Here we note that while this method allows us to investigate feedback from the inclusion of the PMZ on the nucleosynthesis, we cannot investigate the potential feedback on the stellar structure, given that the PMZ is included only in the post-processing. This needs to be kept in mind particularly in relation to the case when the ^{13}C pocket is ingested in the following TP (as detailed in the next section), which could lead to modification of the TP structure (Bazan & Lattanzio 1993).

We employed a network of 320 nuclear species from neutrons and protons up to bismuth. Nuclear reaction rates were included using the *reaclib* file provided by the Joint Institute for Nuclear Astrophysics (JINA, Cyburt et al. 2010), as of May 2012 (*reaclib_V2.0*). The rates of the neutron source reactions correspond to Heil et al. (2008) for the $^{13}\text{C}(\alpha, n)^{16}\text{O}$ and to Iliadis et al. (2010) for the $^{22}\text{Ne}(\alpha, n)^{25}\text{Mg}$ and $^{22}\text{Ne}(\alpha, \gamma)^{26}\text{Mg}$ reactions. For the neutron-capture cross sections, the JINA *reaclib* database includes the KADoNiS database (Dillmann et al. 2006)².

3.2.1 The inclusion of the PMZ

We test the effect of different types of PMZs on the resulting ^{13}C pockets and the ensuing nucleosynthesis. Our abun-

² We used the rates labelled as *ka02* in the JINA database (instead of *kd02*) as they provide the best fits to KADoNiS at the temperature of interest for AGB stars.

dance profiles within the PMZ are constructed in the following way. As commonly assumed, we postulate that the PMZ is the result of mixing occurring below the bottom of the convective envelope during each TDU episode at the point in time when the envelope reaches its maximum inward penetration in mass. We define that the mixing extends for a depth M_{PMZ} , in other words, that it reaches down to a point in mass of M_{PMZ} below the base of the convective envelope. To describe the mixing function over mass we scale the mass coordinate within the PMZ to a variable m_{scaled} that varies between 0 and 1 over the PMZ:

$$m_{\text{scaled}} = \frac{m - m_{\text{base}}}{m_{\text{top}} - m_{\text{base}}} \quad (2)$$

where m is the mass variable within the PMZ, m_{top} is the mass at the top of the PMZ (i.e., the mass coordinate of the base of the convective envelope) and m_{base} is the mass at the base of the PMZ (i.e., $m_{\text{base}} = m_{\text{top}} - M_{\text{PMZ}}$).

The mixing function is defined as the exponential 10^f , where in the “standard” case f is a linear function of the mass:

$$f = 4 m_{\text{scaled}} - 4 \quad (3)$$

Clearly, at the top of the PMZ ($m_{\text{scaled}} = 1$) $10^f = 1$ and at the base ($m_{\text{scaled}} = 0$) $10^f = 10^{-4}$. Below $m_{\text{scaled}} = 0$ we include no mixing. Finally, we determine the mixed abundances of all species X_i in the PMZ using mass conservation:

$$X_i(m) = 10^f X_i(\text{CE}) + (1 - 10^f) X_i^{\text{intershell}}(m), \quad (4)$$

where $X_i^{\text{intershell}}(m)$ are the original abundances in the intershell and $X_i(\text{CE})$ the abundances at the base of the convective envelope. Because $X_{\text{H}}^{\text{intershell}}(m) = 0$, for protons the equation becomes simply:

$$X_{\text{H}}(m) = 10^f X_{\text{H}}(\text{CE}) \quad (5)$$

which, in logarithmic scale, yields a line connecting $X_{\text{H}}(\text{CE})$ at m_{top} and $10^{-4} X_{\text{H}}(\text{CE})$ at m_{base} (top panel of Fig. 1).

We use $M_{\text{PMZ}} = 2 \times 10^{-3} M_{\odot}$ in most of our calculations, which is within the typical range required to match the observation that *s*-process enriched AGB stars of metallicity around solar show Ba abundances on average roughly ten times higher than solar (Smith & Lambert 1990; Busso et al. 1995; Lambert et al. 1995; Busso et al. 2001). Models where this parameter has been modified can be found, e.g., in Karakas & Lugaro (2016). In the present paper, we will discuss in detail the differences and the connections between varying M_{PMZ} and varying the mixing profile, f .

In Fig. 1 we show the standard PMZ included at the deepest extent of the first TDU of the $1.25 M_{\odot}$ $Z = 0.01$ model and the resultant ^{13}C pocket. This case is used as an illustrative example in the rest of this section and it is typical. The figure also illustrates our definition of the mass width of ^{13}C pocket (M_{pocket}), as the mass width within the PMZ where the mole fraction of ^{13}C is greater than the mole fraction of ^{14}N , and the total effective mass of ^{13}C in the pocket, $M_{\text{tot}}(^{13}\text{C}_{\text{eff}})$. The effective mass fraction of ^{13}C at each given mass point is defined following Cristallo et al. (2009) as $X^{13}\text{C}_{\text{eff}} = X_{13} - X_{14} \frac{13}{14}$, where X_{13} and X_{14} are

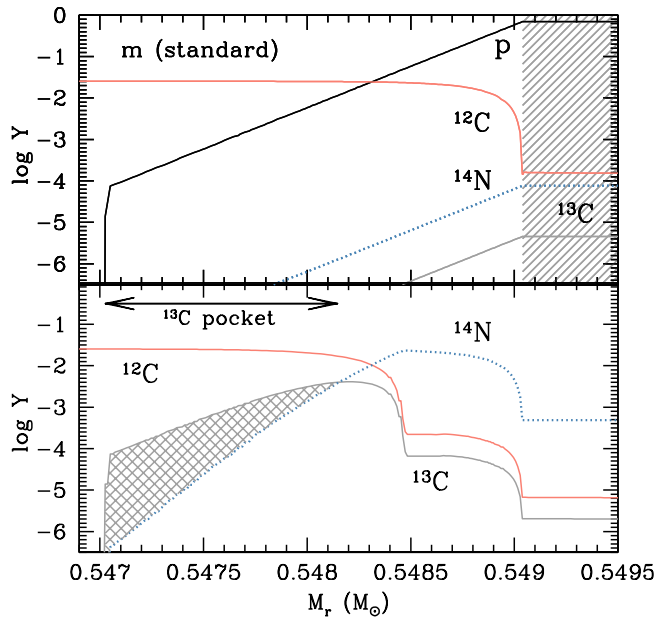


Figure 1. Profile of selected isotopes derived using the standard exponential mixing function as applied to the $1.25 M_{\odot}$ $Z = 0.01$ model at the deepest extent of the first TDU episode. Top panel: the proton profile just after insertion of the PMZ, the shaded region represents the convective envelope. Bottom panel: the ^{13}C and ^{14}N pockets formed after all protons have burnt. The cross hatched region represents $M_{\text{tot}}(^{13}\text{C}_{\text{eff}})$ and the double arrow indicates M_{pocket} , as defined in the text.

the mass fractions of ^{13}C and ^{14}N , respectively. This definition is required because, as mentioned above, ^{14}N is a strong neutron poison via the $^{14}\text{N}(n,p)^{14}\text{C}$ reaction. Integrating $X^{13}\text{C}_{\text{eff}}$ over M_{pocket} we obtain $M_{\text{tot}}(^{13}\text{C}_{\text{eff}})$.

We examined two types of variations from the standard profile: the shape of the mixing profile (Set 1) and the introduction of a discontinuity at the top of the PMZ (Set 2). In Set 1 we consider the different shaped profiles shown in the left panels of Fig. 2. They take the following forms (as compared to Eq. 3) and we will refer to them hereafter using the shorts labels indicated in brackets:

$$f = 4m^3_{\text{scaled}} - 4, \quad (m^3) \quad (6)$$

$$f = 4m^2_{\text{scaled}} - 4, \quad (m^2) \quad (7)$$

$$f = 4m_{\text{scaled}} - 4, \quad (m, \text{i.e., standard}) \quad (8)$$

$$f = 4m^{1/2}_{\text{scaled}} - 4, \quad (m^{1/2}) \quad (9)$$

$$f = 4m^{1/3}_{\text{scaled}} - 4, \quad (m^{1/3}) \quad (10)$$

Table 2 shows M_{pocket} , also in form of percentage of the total mass of the PMZ, and $M_{\text{tot}}(^{13}\text{C}_{\text{eff}})$ for the different mixing functions. In Set 1 M_{pocket} decreases when decreasing the exponent on the mass, however, $M_{\text{tot}}(^{13}\text{C}_{\text{eff}})$ presents a maximum for the standard case because when the exponent on the mass decreases the size of the ^{14}N pocket increases. The m^2 case appears to produce the proton profile most similar to those obtained by Cristallo et al. (2009) for their most efficient choice of $\beta = 0.1$ (see, e.g., their Fig. 2). For their $2 M_{\odot}$ model with $Z = 0.0138$, Cristallo et al. (2009) finds $M_{\text{PMZ}} \simeq 10^{-3}$, $M_{\text{pocket}} = 5.54 \times 10^{-4} M_{\odot}$ and $M_{\text{tot}}(^{13}\text{C}_{\text{eff}})$

Table 2. Properties of the ^{13}C pockets for the different mixing profiles. Masses are all in M_{\odot} .

Profile	M_{pocket} (10^{-3})	% of M_{PMZ}	$M_{\text{tot}}(^{13}\text{C}_{\text{eff}})$ (10^{-6})
Set 1			
m^3	1.70	85%	8.58
m^2	1.53	77%	9.92
m	1.16	58%	11.6
$m^{1/2}$	0.67	33%	9.31
$m^{1/3}$	0.40	20%	5.97
Set 2			
m	1.16	58%	11.6
$-m$	1.53	76%	15.2
$-2m$	1.99	99%	20.5
$-3m$	2.00	100%	6.33

$= 7.38 \times 10^{-6} M_{\odot}$. These number are close to those obtained with our definition of the mixing function for Set 1, however, it should be kept in mind that the values calculated by Cristallo et al. (2009) change for different TDU episodes as the physical properties at the base of the convective envelope change and feedback onto the features of the PMZ (see, e.g., their Fig. 8). This effect is not considered in our parameteric models, where the same PMZ is inserted at each TDU. Interestingly, the fact that the final s -process results are very similar (as discussed at length by, e.g., Karakas & Lugaro 2016) indicates that this structure feedback is second-order effects.

In Set 2, we examine models where a discontinuity is included at the top of the PMZ as shown in the right panels of Fig. 2, and with features listed in Table 2. We construct these profiles as follows (with short notation in brackets):

$$f = 3m_{\text{scaled}} - 4, \quad (-m) \quad (11)$$

$$f = 2m_{\text{scaled}} - 4, \quad (-2m) \quad (12)$$

$$f = m_{\text{scaled}} - 4, \quad (-3m) \quad (13)$$

Among these profiles, the $-3m$ profile is very similar to that obtained by mixing due to magnetic fields (see Fig. 2 of Trippella et al. 2016) and the $-m$ case produces a $^{13}\text{C}_{\text{eff}}$ profile which is the closest to the TAIL case presented by Cristallo et al. (2015) (see their Figure 7).

In general, in the Set 2 profiles fewer protons are mixed than in the Set 1 profiles, which results in a lower amount of ^{14}N and a larger M_{pocket} . A higher $M_{\text{tot}}(^{13}\text{C}_{\text{eff}})$ is also obtained, except for the $-3m$ case, where the lowest number of protons are mixed.

4 RESULTS

4.1 Neutron density and neutron exposure during the AGB phase

The initial stellar mass and metallicity determine the main evolutionary features during the AGB phase, and these in turn determine which neutron source is activated, how the ^{13}C burns, the resulting neutron density N_n , and total number of free neutrons. The latter is usually measured via the

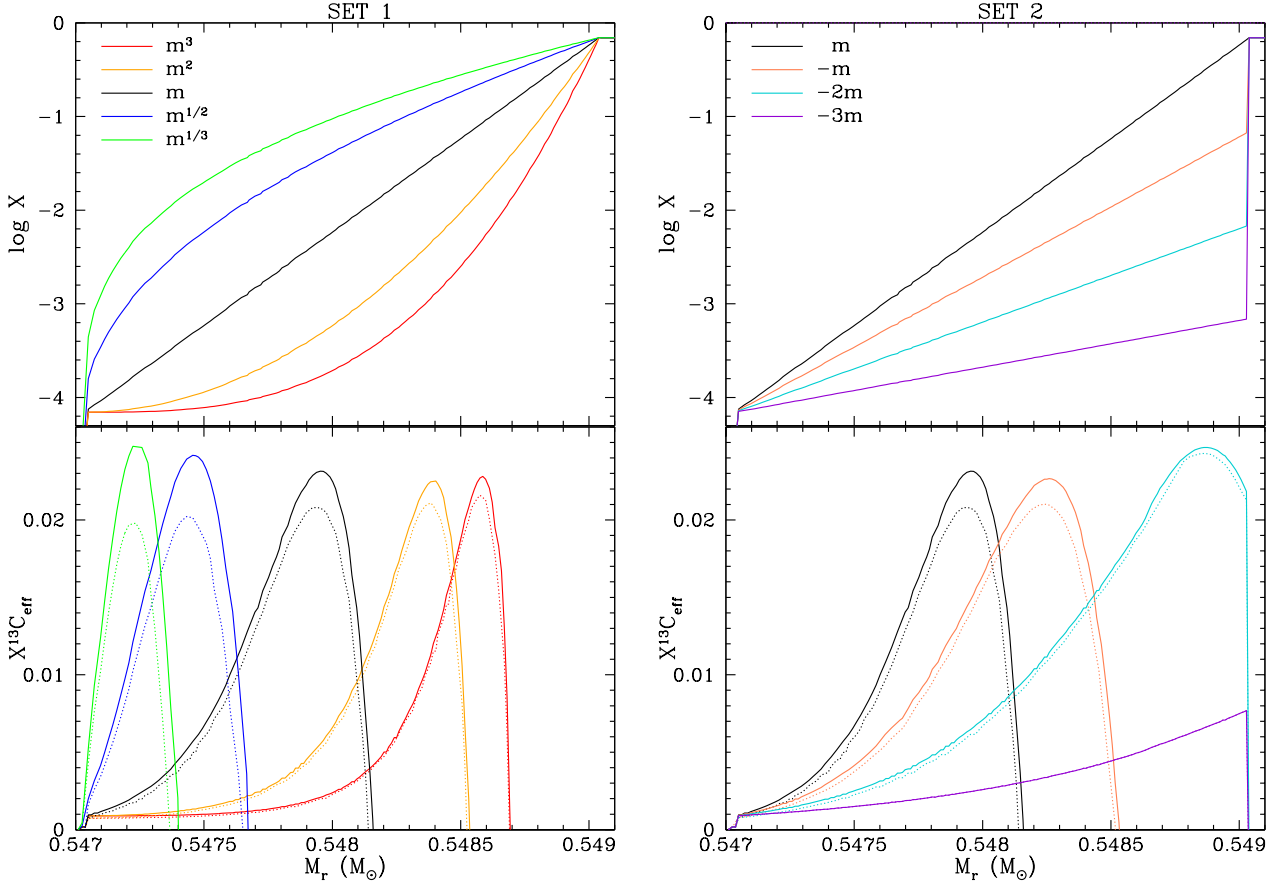


Figure 2. Proton profiles (top panels) and resultant ^{13}C mass fractions (bottom panels) obtained by introducing different shapes of the mixing function of the PMZ at the deepest extent of the first TDU episode of the $1.25 M_{\odot}$ $Z=0.01$ model. Note that the peak in the ^{13}C mass fraction moves in mass for the different cases because it is always located where $\log X_p = -2.5$. Above this value of $\log X_p$, ^{13}C is converted into ^{14}N . The dotted lines in the bottom panels show the amount of ^{13}C remaining at the onset of the next TP, and subsequently ingested in the TP, a specific feature of the $1.25 M_{\odot}$ $Z=0.01$ model (see text for details).

neutron exposure τ , defined as the time-integrated neutron flux $\int N_n v_T dt$, where v_T is the thermal velocity.

A summary of the sources of the neutron fluxes present during the AGB phase in the different models is presented in Table 3 (see also Lugaro et al. 2012, for a detailed description of the different regimes). In relation to the ^{13}C pocket we find in our models both the uncommon case, specific to stars of low mass and high metallicity where some ^{13}C is left in the pocket and burns while ingested in the next TP (^{13}C ingestion Cristallo et al. 2009), as originally proposed as the standard scenario (Iben & Renzini 1982) and the common case where all the ^{13}C in the pocket burns in radiative conditions before the onset of the next TP (^{13}C radiative, as discovered by Straniero et al. 1995). At low mass and metallicity, we also find a few instances of proton ingestion episodes directly inside the TPs. These protons produce extra ^{13}C and neutrons. For stars of mass higher than roughly $3 M_{\odot}$, when the maximum temperature in the intershell reaches above 300 MK (see Table 1), neutrons are also released by the ^{22}Ne neutron source inside the TPs (^{22}Ne burning).

In Fig. 3 we show, for three representative stellar models calculated using Set 1, the evolution as a function of time of the maximum N_n within the whole star, which is the best proxy to identify the different significant neutron flux

Table 3. Summary of the sources of the neutron fluxes experienced by the different stellar models.

Mass	Z	^{13}C radiative	^{13}C ingestion	proton ingestion	^{22}Ne burning
1.25	0.01		all PMZs		
1.8	0.01	late PMZs	early PMZs		
3.0	0.01	all PMZs			late TPs
3.0	0.02	all PMZs			late TPs
4.0	0.02	all PMZs			late TPs
1.5	0.0001	late PMZs	early PMZs	early TPs	

events along the AGB evolution. Table 4 lists the values of the neutron exposure calculated during selected interpulse periods using the maximum neutron density shown in Fig. 3. We selected early and late ^{13}C pockets during the evolution to show how the neutron flux changes due to both structural and feedback effects along the evolution. We discuss each example star in a separate subsection.

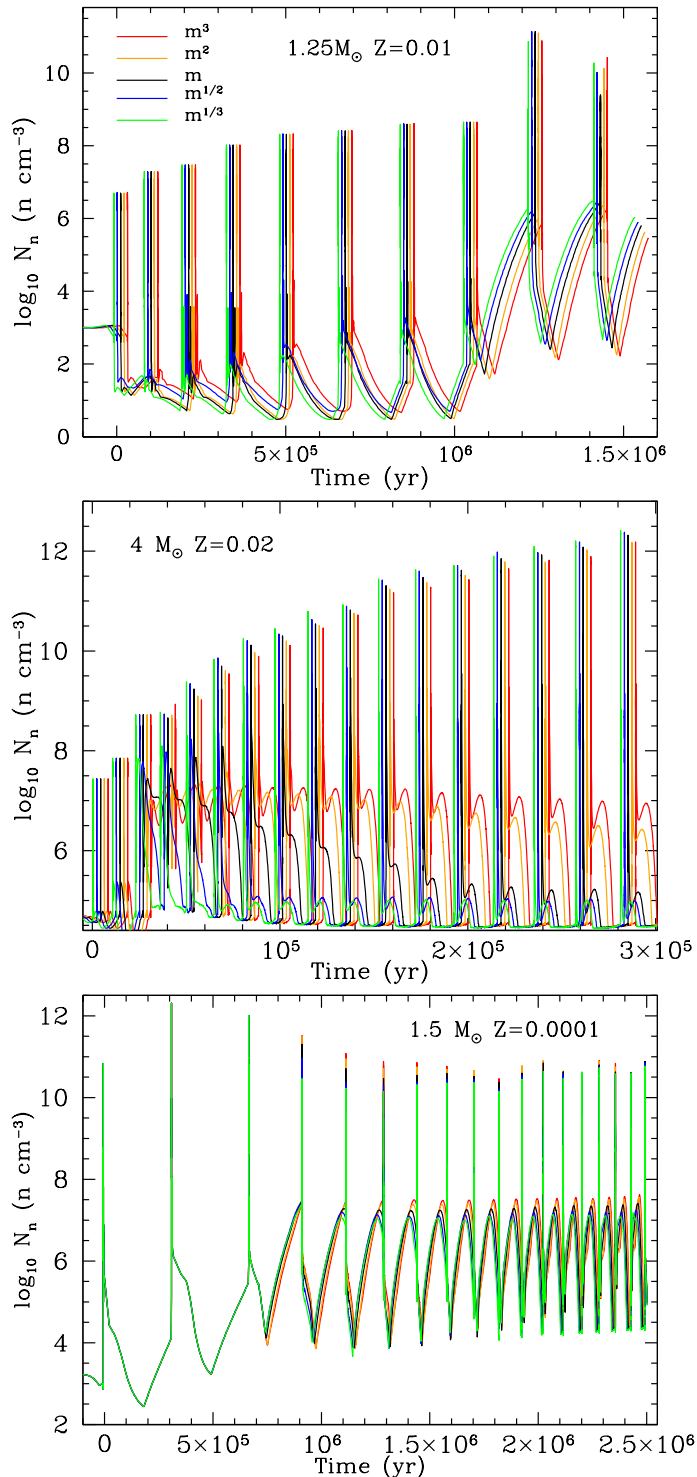


Figure 3. The maximum neutron density within the star as function of time during the thermally pulsing AGB phase of the $1.25 M_{\odot}$ $Z = 0.01$ (top panel), $4 M_{\odot}$ $Z = 0.02$ (middle panel) and $1.5 M_{\odot}$ $Z = 0.0001$ (bottom panel) models for the different cases of Set 1. The zero time is set at the time of the 1st TP for the $m^{1/3}$ case. To be able to distinguish the different cases, the other lines are all slightly offset in time. Spikes in the N_n identify the TPs. Note the difference in the duration of the TP-AGB phase between the models, which increases with decreasing mass and/or metallicity.

Table 4. The neutron exposure τ (in mbarn^{-1}) during the interpulse periods for all the models (M, Z stands for the mass in M_{\odot} and the metallicity of the star). For the models that experience more than five TDUs episodes (hence PMZs) values are given for two different PMZs, selected as representative of an early and a late time during the evolution.

M, Z	PMZ	m^3	m^2	m	$m^{1/2}$	$m^{1/3}$	$-m$	$-2m$	$-3m$
1.25,0.01	1	0.04	0.06	0.10	0.13	0.16	0.06	0.04	0.01
1.8,0.01	5	0.59	0.59	0.58	0.56	0.53	0.68	0.70	0.30
3.0,0.01	1	0.63	0.67	0.71	0.72	0.68	0.80	0.77	0.36
3.0,0.01	16	0.66	0.68	0.74	0.67	0.57	0.78	0.80	0.40
3.0,0.02	1	0.47	0.48	0.50	0.49	0.46	0.59	0.50	0.22
3.0,0.02	15	0.45	0.44	0.42	0.38	0.34	0.54	0.60	0.25
4.0,0.02	1	0.54	0.57	0.58	0.54	0.48	0.74	0.70	0.35
4.0,0.02	14	0.62	0.69	0.45	0.07	0.04	0.97	1.13	0.50
1.5,0.0001	1	2.35	2.78	3.64	3.95	3.34	4.03	3.45	2.03
1.5,0.0001	15	2.58	2.31	1.87	1.42	1.23	3.38	4.25	2.80

4.1.1 The $1.25 M_{\odot}$ $Z=0.01$ model

The spikes in the neutron density in the top panel of Fig. 3 clearly show the 10 TPs experienced by this model. The N_n spikes corresponding to the first 8 TPs represent the signature of the convective burning of the ^{13}C from the H-burning ashes, resulting in a low neutron density (10^{7-8} cm^{-3}) and insignificant neutron exposure. After the 8th TP, a TDU episode occurs and the PMZ is inserted. At this point the radiative burning of ^{13}C is noticeable as a smooth increase in N_n during the interpulse periods. However, due to temperatures in the pocket being below 80 MK, only a small fraction of ^{13}C burns before the onset of the following TP and a significant amount of ^{13}C is still left when the next TP occurs. As shown in the bottom panels of Fig. 2 this fraction depends on the PMZ case used, with a higher fraction left for the case m^3 , which has the both the lowest local abundance of ^{13}C - the rate of the $^{13}\text{C}(\alpha, n)^{16}\text{O}$ reaction is proportional to the number of ^{13}C nuclei - and the maximum value of ^{13}C located at the highest mass, where the temperature is lower.

The difference in the ^{13}C fraction left to be ingested between the different Set 1 cases is reflected in the values of the neutron exposures during the interpulse periods, which increase from 0.04 mbarn^{-1} for case m^3 to 0.16 mbarn^{-1} for case $m^{1/3}$ (Table 4). The ingestion of the ^{13}C (and ^{14}N) pocket in the following TPs produces a higher spike in N_n during the last 2 TPs than in the previous TPs, up to roughly 10^{11} cm^{-3} , depending on the TP and the PMZ case considered - i.e., depending on the interplay of the $^{13}\text{C}(\alpha, n)^{16}\text{O}$, $^{14}\text{N}(\alpha, \gamma)^{18}\text{F}$, $^{14}\text{N}(n, p)^{14}\text{C}$ reactions, and the mixing timescale as different ^{13}C and ^{14}N abundances are ingested in the TPs.

Also the $1.8 M_{\odot}$ $Z = 0.01$ model experiences a few ^{13}C ingestions during the early TPs, however, their overall effect is much smaller than in the case of the $1.25 M_{\odot}$ $Z = 0.01$. The neutron exposure in the ^{13}C pocket during the interpulse periods for this model is $\sim 0.60 \text{ mbarn}^{-1}$, very close to that experienced by the $3 M_{\odot}$ $Z = 0.01$ model ($\sim 0.70 \text{ mbarn}^{-1}$), which does not suffer any ^{13}C ingestion. In

these cases, where ^{13}C radiative burning is the main mode of neutron production, the neutron exposure in the ^{13}C pocket does not change significantly with the mixing profile because it is controlled by the maximum value of $X^{13}\text{C}_{\text{eff}}$, which is relatively constant (Fig. 2), although feedback effects play a role in some of the models, as discussed below.

4.1.2 The $4 M_{\odot}$ $Z=0.02$ model

The middle panel of Fig. 3 shows the evolution of the maximum neutron density during the 17 TPs experienced by this model for the different cases of Set 1. As the TP temperature increases during the evolution, the effect of the ^{22}Ne neutron source becomes more visible in the later TPs, where N_n reaches above 10^{12} cm^{-3} . The N_n in the TPs increases from the m^3 to the $m^{1/3}$ cases because the ^{14}N pocket becomes larger and contributes to the abundance of ^{22}Ne in the TPs, increasing the rate of the $^{22}\text{Ne}(\alpha, n)^{25}\text{Mg}$ reaction.

Distinct differences are present in the N_n produced in the ^{13}C pocket during the interpulse periods for the different Set 1 cases: the two most extreme cases m^3 and $m^{1/3}$ show neutron densities during the slow burning phase within the interpulse periods typically as high as 10^7 and as low as 10^5 cm^{-3} , respectively. The reason is a combination of two factors: (1) depending on the choice of the PMZ profile the maximum ^{13}C abundance is located closer to (e.g., case m^3) or further from (e.g., case $m^{1/3}$) the bottom of the envelope (Fig. 2) and (2) the temperature in the region where the PMZ is inserted is a steep function of the location in mass and is much higher in the $4 M_{\odot}$ model than in the lower mass models (Fig. 4). It follows that in the $m^{1/2}$ and $m^{1/3}$ cases, which form the ^{13}C pocket deeper in the star than the other cases, ^{13}C is immediately exposed to the temperatures at which the $^{13}\text{C}(\alpha, n)^{16}\text{O}$ reaction is activated. A spike in the neutron density occurs already on a very short timescale in correspondence to the introduction of the PMZ (in the figure, the spike is very close to the spike corresponding to the previous TP produced by the ^{22}Ne neutron source). This effect becomes even more pronounced as the star evolves and the temperature increases (Fig. 4). In the late TPs for the $m^{1/2}$ and $m^{1/3}$ cases, the temperature at which the PMZ is inserted is so high that the CN cycle is established, ^{13}C is quickly transmuted into ^{14}N , and the amount of ^{13}C becomes smaller (e.g., M_{pocket} decreases by a factor of five or so). In this situation the neutron flux is effectively inhibited, and the neutron exposure becomes lower than 0.1 mbarn^{-1} for the $m^{1/2}$ and $m^{1/3}$ cases (see Table 4). In the m^2 and m^3 cases, instead, the fewer number of protons mixed do not lead to the same very efficient burning at the time of the formation of the PMZ and a higher neutron flux results during the interpulse periods. The m proton profile is an intermediate case, which also shows the effect of the time evolution of the temperature within each PMZ and the ^{13}C pocket. When the PMZ is inserted, the temperature is high enough to activate the $^{13}\text{C}(\alpha, n)^{16}\text{O}$ reaction and a spike in the N_n is seen. As the envelope recedes after the TDU, the temperature decreases, to start increasing again from the start of the activation of the H-burning shell.

Finally, we note that the $4 M_{\odot}$ $Z = 0.02$ model reaches 40 MK at most at the base of the envelope during the latest TDUs, which is only borderline to trigger the ‘‘hot TDU’’ (Goriely & Siess 2004). In the case of the hot TDU, the CN

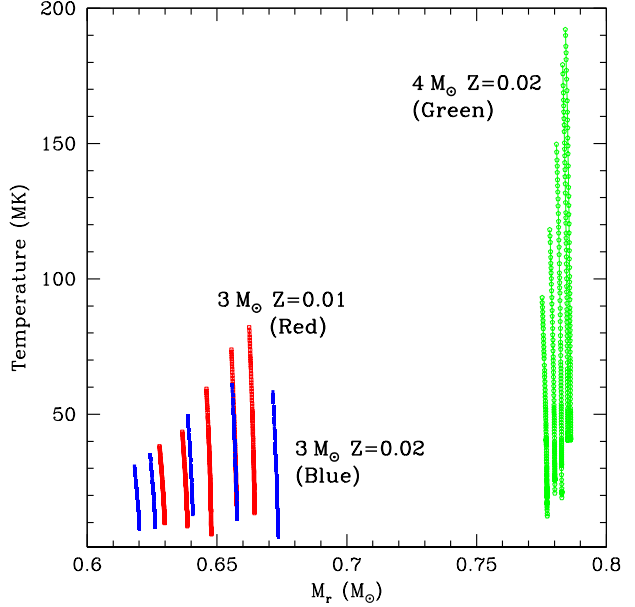


Figure 4. The temperature as a function of mass in the PMZ at the time when the PMZ is inserted for the $3 M_{\odot}$ models of $Z = 0.01$ (red) and 0.02 (blue), and the $4 M_{\odot}$ $Z = 0.02$ model (green). Each line represents the temperature within the PMZ for some representative TDU episodes along the evolution: for the $3 M_{\odot}$ model of $Z = 0.02$ models, the 1st, 2nd, 5th, 10th and 16th TDU, for the $3 M_{\odot}$ $Z = 0.01$ and $4 M_{\odot}$ $Z = 0.02$ models, the 1st, 3rd, 6th, 10th, and 13th TDU, with the TDU number increasing from left to right, i.e., in order of increasing the location in mass coordinate M_r .

cycle is at work during the mixing responsible for the formation of the PMZ and the formation of the ^{13}C pocket is strongly inhibited. In any case, as derived above by comparing, e.g., the $m^{1/3}$ to the m^3 case in the middle panel of Fig. 3 and in Table 4 we find that, strongly depending on the mixing profile, burning processes other than the hot TDU are also at work during the formation of the PMZ, which can suppress the number of neutrons released in the ^{13}C pocket in the $4 M_{\odot}$ model.

4.1.3 The $1.5 M_{\odot}$ $Z=0.0001$ model

The bottom panel of Fig. 3 shows the neutron density as a function of time for the 18 TPs experienced by the $1.5 M_{\odot}$ $Z = 0.0001$ model. The very low metallicity of this model plays an important role in producing three to five times higher neutron exposures than the models of higher metallicity (Table 4) due to the primary nature of the ^{13}C neutron source. The $m^{1/3}$ proton profile produces the largest ^{14}N pocket, which results in a strong enhancement of primary ^{22}Ne in the intershell. The $^{22}\text{Ne}(n, \gamma)^{23}\text{Ne}(\beta^-)^{23}\text{Na}$ reaction chain steals neutrons from the s -process, while increasing the production of Na (see Table 6) with the consequence that the neutron exposures decreases during the evolution ($3.34\text{--}1.23 \text{ mbarn}^{-1}$). Conversely, the m^3 proton profile produces the smallest ^{14}N pocket so the neutron exposure does not significantly changes during the evolution ($2.35\text{--}2.38 \text{ mbarn}^{-1}$). It is also noticeable in Fig. 3 that the early TPs

experience a spike in the neutron density, reaching up to $\sim 10^{12} \text{ cm}^{-3}$ before the PMZ is inserted. We infer these to be caused by mild proton ingestions. Furthermore, the effect of ^{13}C ingestions are visible in the first few TPs after the PMZ is inserted, and explain the fact that the neutron exposure during the interpulse period is smaller for the 2nd ^{13}C pocket than for the last (Table 4). However, the final *s*-process distribution produced by this model is dominated by the effect of the radiative ^{13}C burning, which produces the neutron flux noticeable from the figure in most of the interpulse periods.

4.2 Abundance results for the elements heavier than Fe

In Figs. 5 and 6 we present the elemental abundances in the form $[\text{X}/\text{Fe}]^3$ resulting at the stellar surface at the end of the evolution for all our calculated models. We will focus on the *s*-process elements Sr, Ba, and Pb, as representative of the first, second, and third *s*-process peaks, respectively. We discuss in our analysis the absolute enrichments, i.e., $[\text{Sr}/\text{Fe}]$, $[\text{Ba}/\text{Fe}]$, and $[\text{Pb}/\text{Fe}]$, and the relative abundance distribution, i.e., $[\text{Ba}/\text{Sr}]$ and $[\text{Pb}/\text{Ba}]$, describing the relative height of the three *s*-process peaks. These ratios are reported in Table 5 for all the computed models.

The initial stellar mass and metallicity play the major role in determining the final *s*-process abundances. The stellar structure (mainly the temperature) is responsible for activating the different types of neutron sources, which result in fluxes of neutrons characterised by the different neutron densities and exposures detailed above. We can derive the main differences between the stellar models in terms of both absolute abundances and relative distribution by comparing the standard *m* cases shown in the different panels of Fig. 5. These differences can be summarised as follows: (1) The abundance distribution for the $1.25 M_{\odot}$ is almost fully determined by the ^{13}C ingestions, which produce higher neutron densities and lower neutron exposures than the radiative ^{13}C burning occurring in all the other models. For this reason the final *s*-process distribution is shifted towards the first *s*-process peak at Sr. With respect to the 1.8 and $3 M_{\odot}$ models, the higher neutron density also produces higher $[\text{Rb}/\text{Zr}]$ ratios, due to the activation of the branching point at ^{86}Rb . A further consequence of the ^{13}C ingestions, together with the fact that this model experiences the lowest amount of TDU of all the models (Table 1), is that the absolute abundances are lower by roughly one order of magnitude than in the other models. (2) Because the neutron exposure increases with metallicity, the $1.5 M_{\odot} Z = 0.0001$ model has the highest abundance of the third peak element Pb. It also has the highest absolute abundances by one order of magnitudes. This is mostly due to the normalisation to Fe, which is two orders of magnitude lower than in the other models. Metallicity driven differences are also noticeable in the relative abundance distribution between the $Z = 0.01$ and $Z = 0.02$ models, e.g., the $[\text{Ba}/\text{Sr}]$ ratio is three times higher in the former than the latter. (3) Between the two $Z = 0.02$

models, the $4 M_{\odot}$ model shows a marginally higher enrichment relative to the $3 M_{\odot}$ model in the second and third peaks, by at most 50% relative to the first peak, due to the higher contribution of the ^{22}Ne neutron source.

Overall, it is the combination of the different types of neutron fluxes, their relative contribution, and the efficiency of the TDU that control the final results as a function of the stellar mass and metallicity. On top of these, here we aim to identify and discuss the effects of changing the features of the PMZ for each stellar model.

4.2.1 Comparison of the results from Set 1

The $1.8 M_{\odot} Z = 0.01$ model (top right panel of Fig. 5) is the most representative of the case when the final abundance distribution is predominantly determined by radiative ^{13}C burning. The neutron exposure in the ^{13}C pocket in this model does not change significantly (Table 4) and so do not the relative ratios $[\text{Ba}/\text{Sr}]$ and $[\text{Pb}/\text{Ba}]$, which are controlled by the neutron exposure, and are constant within ± 0.07 dex. On the other hand, the absolute abundances vary by roughly a factor of two. They reach the maximum for the standard *m* case, following the maxima of the M_{pocket} and the $M_{\text{tot}}(^{13}\text{C}_{\text{eff}})$ (Table 2). These results are qualitatively similar to those that would be obtained by varying the M_{PMZ} instead of the mixing profile: the neutron exposure, which controls the relative ratios, does not change; while the absolute amount of matter exposed to the neutron flux, which controls the absolute ratios, changes.

The trend is similar in the $3 M_{\odot} Z = 0.01$ and $Z = 0.02$ models and the $4 M_{\odot} Z = 0.02$ models. In these models – even in the $4 M_{\odot}$ model, where the neutron density presents a complex dependency on the mixing function (Fig. 3) – variations in the relative ratios $[\text{Ba}/\text{Sr}]$ and $[\text{Pb}/\text{Ba}]$ are typically lower than ± 0.2 dex. The most significant difference compared to the $1.8 M_{\odot} Z = 0.01$ model is that in the models of higher mass the ^{22}Ne neutron source is also activated in the late TPs, which generally shift the abundance distribution towards the first *s*-process peak. An indirect effect from the PMZ on the activation of the ^{22}Ne results when a large ^{14}N pocket ($m^{1/2}$ and $m^{1/3}$) is present, increasing the production of ^{22}Ne . Ultimately this leads to a stronger neutron flux in the TP. Depending on the temperature in the TP it is possible to boost the production of Sr with respect to Ba, for example, in the $3 M_{\odot} Z = 0.01$ model; or the production of Ba and Pb with respect to Sr, for example, in the $4 M_{\odot} Z = 0.02$ model. The final *s*-process distribution ultimately depends also on the number of TPs experienced by the model, which is higher in the higher mass models relative to the $1.8 M_{\odot}$ case. A higher number of TPs results in a higher enrichment of the intershell, particularly of ^{22}Ne in the cases where the ^{14}N pocket is larger. More neutrons are captured by ^{22}Ne inside the ^{13}C pocket and the neutron exposure decreases.

In the case of the $1.5 M_{\odot} Z = 0.0001$ model, the decrease in the neutron exposure moving from the more shallow cases (m^2 and m^3) to the more steep ($m^{1/2}$ and $m^{1/3}$, Table 4) results in a decreased production of the second and third peak, with respect to the first peak.

Finally, the $1.25 M_{\odot}$ model is very different from all the others because the neutron flux is dominated by the ^{13}C ingestions. Furthermore, the TDU is not efficient enough to

³ $[\text{X}/\text{Fe}]$ is defined as $\log(N_{\text{X}}/N_{\text{Fe}})_{\text{star}} - \log(N_{\text{X}}/N_{\text{Fe}})_{\odot}$, where N_{X} and N_{Fe} are the abundances by number of element X and of Fe, respectively.

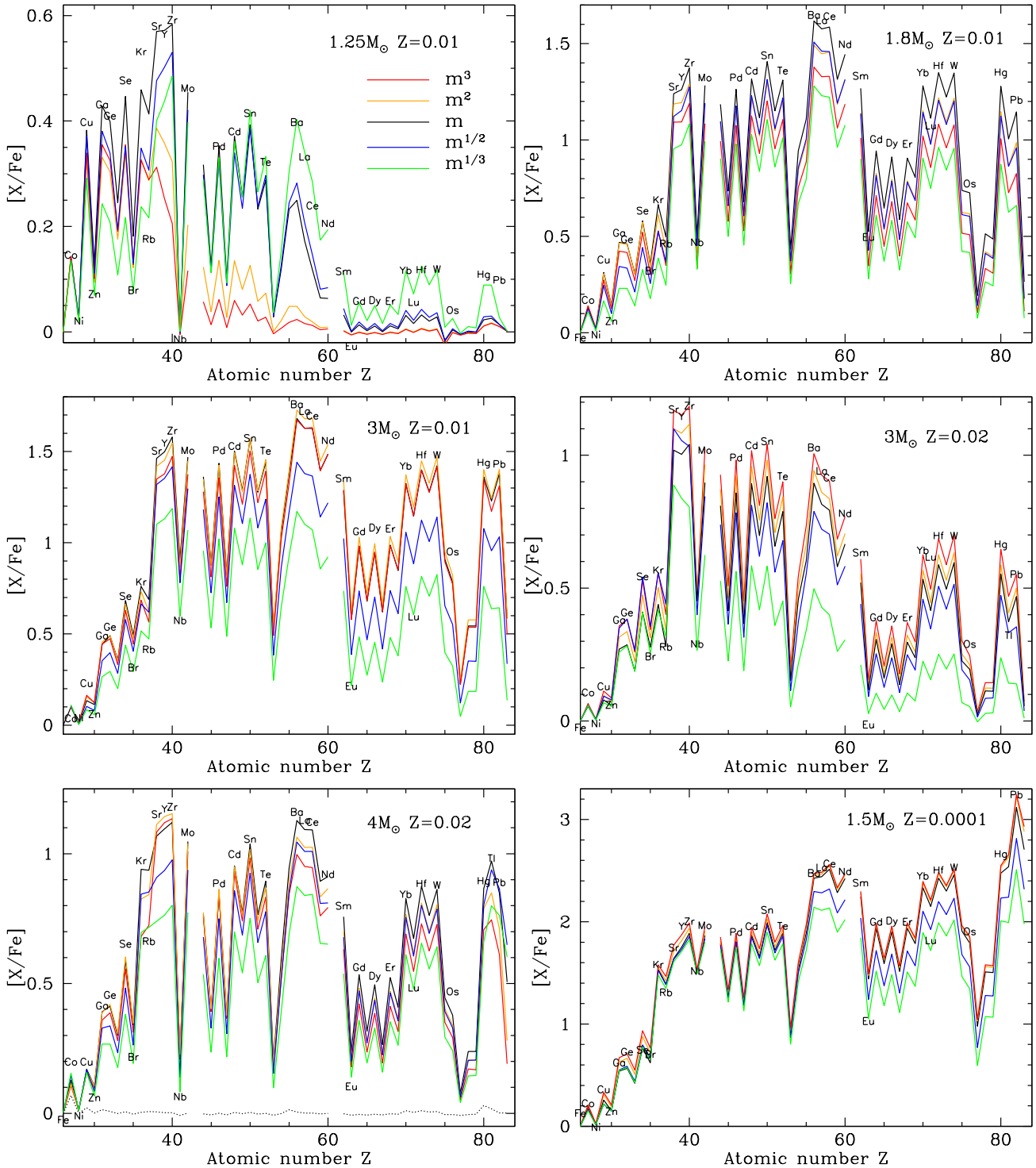


Figure 5. $[X/Fe]$ abundance ratios for the elements from Fe to Bi for the models of Set 1. The gaps in the distribution corresponds to the elements Tc and Pr, which have no stable isotopes. The black dotted line in the $4M_{\odot}$ $Z=0.02$ panel represents the case where no PMZ was included. Note the change of scale for the y-axis between the panels.

produce a strong s -process signature at the stellar surface. Only the first peak elements are observed to be present in the m^2 and m^3 cases. In the other cases some production of Ba is achieved, while the third peak at Pb is never reached. This trend follows that of the neutron exposure in the interpulse (Table 4). The enrichments achieved are not enough

to explain the typical observation for AGB stars of roughly solar metallicity that $[Ba/Fe] \sim 1$, hence, this model may be relevant only for specific applications, e.g., the production of ^{86}Kr (Raut et al. 2013) or, potentially, the composition of Sakurai’s Object, as an alternative to the proton-ingestion episode (Herwig et al. 2011).

Table 5. Selected final surface abundance ratios produced by all the stellar models of Set 1 and Set 2.

Profile	[Sr/Fe]	[Ba/Fe]	[Pb/Fe]	[Ba/Sr]	[Pb/Ba]
1.25 M_⊙ Z=0.01					
m^3	0.31	0.02	0.01	-0.29	-0.01
m^2	0.39	0.05	0.01	-0.34	-0.04
m	0.57	0.25	0.01	-0.32	-0.24
$m^{1/2}$	0.48	0.36	0.02	-0.12	-0.34
$m^{1/3}$	0.40	0.40	0.03	0.00	-0.37
$-m$	0.39	0.05	0.01	-0.34	-0.04
$-2m$	0.62	0.05	0.01	-0.57	-0.04
$-3m$	0.03	0.01	0.01	-0.02	0.00
1.8 M_⊙ Z=0.01					
m^3	1.09	1.38	0.83	0.29	-0.55
m^2	1.19	1.49	0.99	0.30	-0.50
m	1.24	1.62	1.15	0.38	-0.47
$m^{1/2}$	1.12	1.51	0.96	0.39	-0.55
$m^{1/3}$	0.95	1.28	0.66	0.33	-0.62
$-m$	1.37	1.76	1.39	0.39	-0.37
$-2m$	1.38	1.80	1.44	0.42	-0.36
$-3m$	1.07	0.50	0.07	-0.57	-0.43
Test ^a	1.08	0.67	0.06	-0.41	-0.61
3.0 M_⊙ Z=0.01					
m^3	1.35	1.67	1.31	0.32	-0.36
m^2	1.42	1.73	1.40	0.31	-0.33
m	1.46	1.68	1.38	0.22	-0.30
$m^{1/2}$	1.32	1.44	1.03	0.12	-0.41
$m^{1/3}$	1.10	1.17	0.64	0.07	-0.53
$-m$	1.57	1.91	1.72	0.34	-0.19
$-2m$	1.62	2.09	1.99	0.47	-0.10
$-3m$	1.42	1.17	0.62	-0.25	-0.55
3.0 M_⊙ Z=0.02					
m^3	1.17	1.01	0.55	-0.16	-0.46
m^2	1.09	0.94	0.50	-0.15	-0.44
m	1.02	0.89	0.47	-0.13	-0.42
$m^{1/2}$	1.10	0.79	0.35	-0.31	-0.44
$m^{1/3}$	0.89	0.50	0.14	-0.39	-0.36
$-m$	1.44	1.46	1.20	0.02	-0.26
$-2m$	1.49	1.62	1.44	0.13	-0.18
$-3m$	0.89	0.39	0.05	-0.40	-0.34
4.0 M_⊙ Z=0.02					
m^3	1.08	0.99	0.61	-0.09	-0.38
m^2	1.11	1.06	0.71	-0.05	-0.35
m	1.07	1.13	0.85	0.06	-0.28
$m^{1/2}$	0.91	1.04	0.86	0.13	-0.18
$m^{1/3}$	0.74	0.87	0.76	0.13	-0.11
$-m$	1.24	1.34	1.12	0.10	-0.22
$-2m$	1.38	1.55	1.46	0.17	-0.09
$-3m$	0.90	0.60	0.16	-0.30	-0.44
1.5 M_⊙ Z=0.0001					
m^3	1.77	2.47	3.24	0.70	0.77
m^2	1.71	2.48	3.23	0.77	0.75
m	1.64	2.43	3.12	0.79	0.69
$m^{1/2}$	1.63	2.29	2.81	0.66	0.52
$m^{1/3}$	1.61	2.14	2.51	0.53	0.37
$-m$	1.65	2.41	3.34	0.76	0.93
$-2m$	1.61	2.37	3.53	0.76	1.16
$-3m$	1.67	2.45	3.45	0.78	1.00

^aModel run using the same proton profile as from Fig. 2 of Ripplha et al. (2016).

4.2.2 Comparison of the results from Set 2

The cases of Set 2 generally present larger variations in the resulting abundances than the cases of Set 1. In the models of metallicity close to solar where the ^{13}C pocket burns radiatively (1.8, 3, and 4 M_⊙) the main change in the results of the $-m$ and $-2m$ cases relative to the result of the standard m case, is the increase of the absolute abundance production by up to ~ 1 dex. On the other hand, the relative ratios only change within ± 0.1 dex. The reason is that, similarly to Set 1, the main effect of changing the profile in the way described by $-m$ and $-2m$ is to increase M_{pocket} . Again, this is equivalent to increasing the total extent of the PMZ. The maximum of the absolute abundance follows the maximum M_{pocket} and $M_{\text{tot}}(^{13}\text{C}_{\text{eff}})$, corresponding to case $-2m$. The effect of the ^{14}N pocket to increase the ^{22}Ne abundance in the intershell is much milder in Set 2 than in Set 1 because the ^{14}N pocket is a much smaller fraction of the PMZ (Table 2).

As in Set 1, the 1.25 M_⊙ case characterised by the ^{13}C ingestions behaves differently. The results for the $-m$ case are very similar to those from the m^2 case. Instead, in the $-2m$ case the peak of ^{13}C is located at higher mass coordinate within the ^{13}C pocket, i.e., at lower temperatures than those found deeper in the pocket. This means that effectively all the ^{13}C in this case is ingested in the TPs (Fig 2), which results in a lower neutron exposure and the production of the elements between Fe and Sr.

With the $-3m$ case we enter a different regime. In this case the abundance of protons in the PMZ is below 10^{-3} all throughout the PMZ, hence the mass fraction of ^{13}C is below 0.01 everywhere in the pocket (Fig. 2). The comparison of this case with the $m^{1/3}$ case from Set 1 illustrates very clearly why $M_{\text{tot}}(^{13}\text{C}_{\text{eff}})$ cannot be used to uniquely constraint the final s -process distribution. In fact, $M_{\text{tot}}(^{13}\text{C}_{\text{eff}})$ is very similar in the $-3m$ and $m^{1/3}$ cases, however, the final abundances and their relative patterns are completely different. This is due to way the ^{13}C is distributed throughout the pocket (Fig. 2). In the $m^{1/3}$ case, there is a peak in the abundance of ^{13}C of $\simeq 0.25$, in mass fraction. In the $-3m$ case, instead, the maximum abundance of ^{13}C is $\simeq 0.008$, in mass fraction, i.e., roughly 3 times lower. In all the models where the ^{13}C radiative burning is predominant, it is this *local* abundance of ^{13}C that determines the neutron exposure and the final distribution. The abundances resulting from the 1.8, 3, and 4 M_⊙ models, are generally the lowest in the $-3m$ case, and the relative distribution is shifted towards the first s -process peak.

In the case of the 1.25 M_⊙ model, the variations between the $-3m$ and the m cases are even stronger than for the other models, probably due to the interplay between the rate of the $^{13}\text{C}(\alpha, n)^{16}\text{O}$ and of the $^{14}\text{N}(\alpha, \gamma)^{18}\text{F}$ reactions, the latter removing the neutron poison ^{14}N , and the ingestion timescale, which is longer for the $-3m$ case, given that the ^{13}C pocket is spread over a mass four times larger than in the $m^{1/3}$ case.

In the case of the 1.5 M_⊙ model of low metallicity the effect is different. Because of the much lower number of Fe seeds, even the lowest concentration of ^{13}C of case $-3m$ produces a significant neutron exposure, able to reach the third s -process peak.

Due to the similarity of the $-3m$ proton profile to that

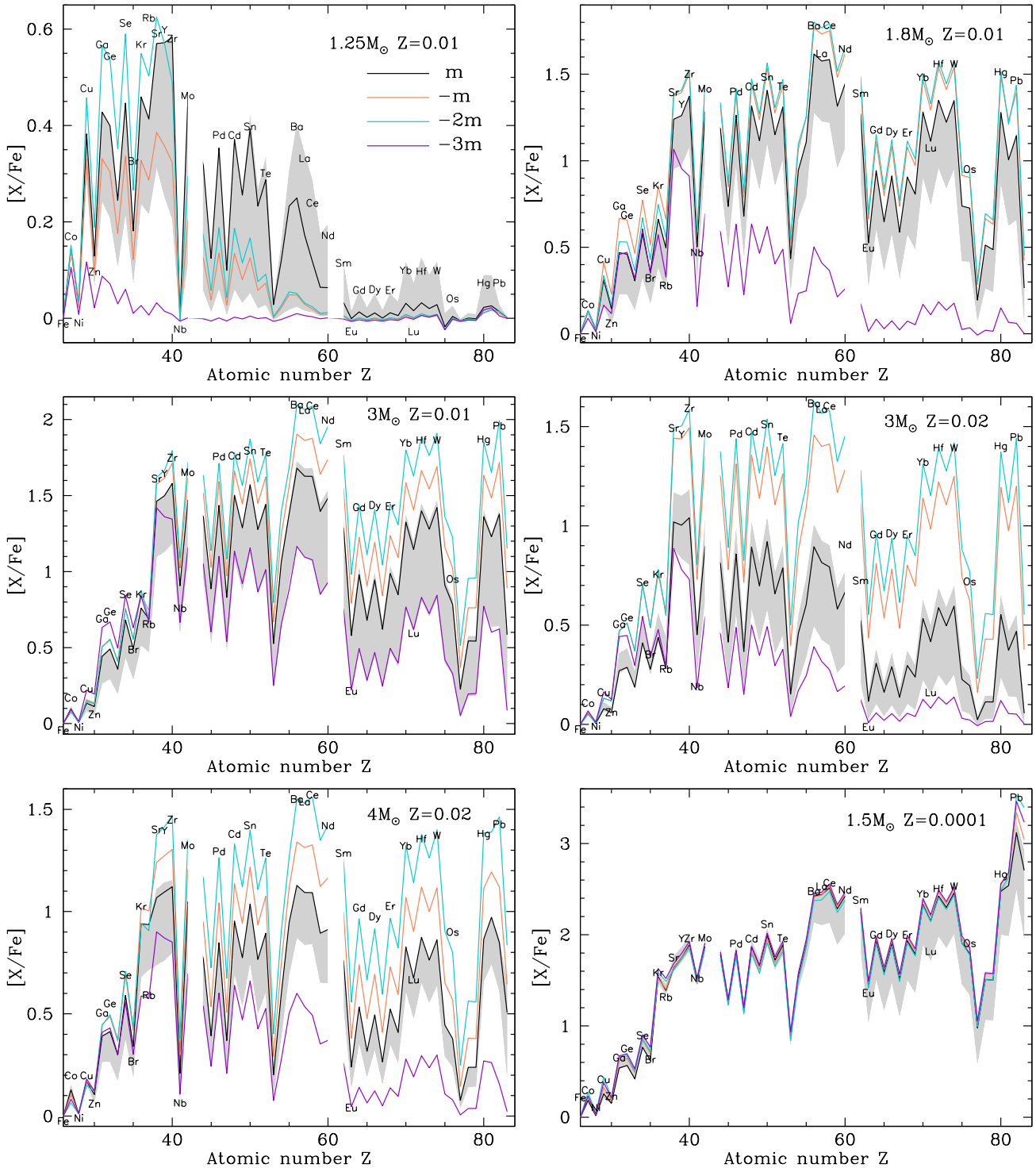


Figure 6. Same as Fig. 5 but for the models from Set 2. For comparison, the grey shaded region represents the spread in abundance predictions from the Set 1 results.

produced by mixing driven by magnetic fields, to test the model uncertainties we further computed a $1.8 M_{\odot}$ $Z = 0.01$ model (case Test in Table 5) using a polynomial fit of the profile shown in Fig. 2 of Trippella et al. (2016). We find that the resulting ratios are extremely similar to those of the $-3m$ case. In half of the PMZ of Trippella et al. (2016) the proton abundance is lower than 10^{-4} . This results in a mass

fraction of ^{13}C lower than 10^{-3} , and a local neutron exposure lower than $\sim 0.05 \text{ mbarn}^{-1}$ (see Fig. 4 of Lugaro et al. 2003a). Such neutron exposure does not produce any significant amount of s -process elements and confirms that our approximation of setting the proton value to zero below $10^{-4} X_{\text{H}}(CE)$ is valid. From Fig. 3 of Trippella et al. (2016), one can derive $[\text{Ba}/\text{Sr}] \sim 0$ (i.e., the solar system abundance

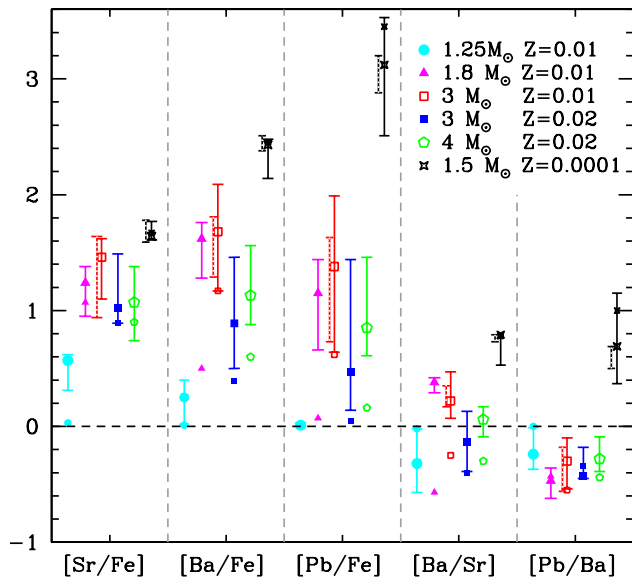


Figure 7. Summary of the selected final abundance ratios for the different stellar models. The large symbols represent the standard case m , and the solid-line error bars represent the spread in values from all the models of Set 1 and Set 2, except for the $-3m$ model, plotted instead as a smaller symbol. Also shown are the ratios obtained with the standard m mixing profile but different values of M_{PMZ} (dashed error bars) for the $3 M_{\odot}$ $Z = 0.01$ model (with M_{PMZ} from 5×10^{-4} to $4 \times 10^{-3} M_{\odot}$) and for the $1.5 M_{\odot}$ $Z = 0.0001$ model (with M_{PMZ} from 6×10^{-4} to $4 \times 10^{-3} M_{\odot}$, from Lugaro et al. 2012).

distribution) and $[\text{Pb}/\text{Ba}] \simeq -0.3$ in the intershell at the end of the evolution of a $1.5 M_{\odot}$ star of $[\text{Fe}/\text{H}] = -0.15$. These values are different from those that we obtain at the end of the evolution in the intershell: $[\text{Ba}/\text{Sr}] = -0.38$ and $[\text{Pb}/\text{Ba}] = -0.97$ (essentially no Pb is produced in our model⁴). The origin of these differences is unclear since on top of implementing exactly the same proton profile we have used the same metallicity. The initial stellar masses are very close to each other (1.8 versus $1.5 M_{\odot}$) and low enough to ensure that the ^{22}Ne neutron source does not play any role. One possibility is the different number of PMZ inserted: 5 in our model and 9 in the case of Trippella et al. (2016). However, the intershell abundance distribution in our model has reached an asymptotic limit by the end of the computed evolution: at the previous interpulse period the $[\text{Ba}/\text{Sr}]$ and $[\text{Pb}/\text{Ba}]$ ratios are within 0.15 dex of their final values and we do not expect any large variations if the evolution was extended.

5 DISCUSSION

The s -process results from our stellar models calculated with a variety of mixing profiles leading to the formation of the ^{13}C pocket are summarised in Fig. 7. A main finding is that for the models of metallicity around solar in which the predominant neutron flux is produced by the ^{13}C pocket burning radiatively, the effect of changing the mixing profiles is in first approximation equivalent to changing the mass extent of the PMZ, M_{PMZ} . The absolute abundances increase with the extent of the ^{13}C pocket, M_{pocket} , e.g., the $-2m$ case dominates the upper limits of the absolute abundance ratios, while the $m^{1/3}$ case dominates the lower limits. For the $-3m$ case the abundances are even lower and are plotted as a separate symbol in Fig. 7. Variations reach up to roughly ± 0.5 dex. On the other hand, the relative ratios do not change within ± 0.2 dex. This result is summarised and illustrated by the 1.8, 3, and $4 M_{\odot}$ models shown in Fig. 7, together with the results obtained for the $3 M_{\odot}$ $Z = 0.01$ model calculated with the standard m mixing profile but different values of M_{PMZ} : the range of variation is the same when changing the mixing profile and when changing M_{PMZ} .

The $1.25 M_{\odot}$ $Z = 0.01$ is different from the others in that the effect of the mixing profile is much more limited: both absolute and relative ratios vary at most by ± 0.2 dex. In this model the prominent effect is the ingestion of the ^{13}C pocket, which somewhat suppresses the neutron flux and produces a different abundance pattern and milder s -process signatures. According to Bazan & Lattanzio (1993), feedback effects from the ingestion onto the stellar structure would lead to higher neutron density and lower neutron exposures than what we have calculated here. The abundance pattern would depart from that resulting from the ^{13}C burning radiative cases in the same way as we have found here, but to a larger extent.

In the low-metallicity $1.5 M_{\odot}$ $Z = 0.0001$ model instead variations due to changing the mixing profile are larger than those obtained by changing the value of M_{PMZ} (Fig. 7). The most significant effects are seen on Pb because in this model the neutron exposure is high enough to produce fixed, equilibrium abundances of Sr and Ba. The $[\text{Pb}/\text{Ba}]$ ratio varies by almost an order of magnitude, with the highest value (1.16) achieved for the $-2m$ profile and the lowest (0.37) with the $m^{1/3}$ profile. This makes variations in the mixing profile at low metallicity one of the possible factors that could contribute to explaining the variations in $[\text{Pb}/\text{Ba}]$ (within a similar range as found here) observed in carbon-enhanced metal-poor (CEMP) stars with enhancements in the s -process elements (Van Eck et al. 2003; Bisterzo et al. 2010, 2011, 2012; Lugaro et al. 2012).

One problem related to CEMP stars is that the standard m models that produce $[\text{Pb}/\text{Ba}] \sim 1$ typically result in $[\text{Na}/\text{Ba}]$ ratios more than an order of magnitude higher than observed (see Fig. 9 of Lugaro et al. 2012). Among the elements lighter than Fe, Na is the only one whose abundance changes significantly for the different profiles tested here

⁴ Note that at the stellar surface we obtain instead $[\text{Ba}/\text{Sr}] = -0.41$ and $[\text{Pb}/\text{Ba}] = -0.61$ (Table 5). The difference between the intershell and the surface $[\text{Pb}/\text{Ba}]$ values is due to the signature of the envelope matter of solar distribution in the surface value, which brings the $[\text{Pb}/\text{Ba}]$ ratio closer to zero.

Table 6. The [Na/Fe], [Na/Ba], and [Pb/Ba] ratios for the $1.5 M_{\odot}$ $Z = 0.0001$ model and the cases of Set 1 and Set 2.

	m^3	m^2	m	$m^{1/2}$	$m^{1/3}$	$-m$	$-2m$	$-3m$
[Na/Fe]	1.86	2.01	2.28	2.54	2.66	1.91	1.61	1.55
[Na/Ba]	-0.61	-0.47	-0.15	0.25	0.52	-0.50	-0.76	-0.90
[Pb/Ba]	0.77	0.75	0.69	0.52	0.37	0.93	1.16	1.00

(Table 6). This is because ^{23}Na (the only stable isotope of Na) is produced in the H-burning shell and in the top layers of the PMZ by proton captures on ^{22}Ne and in the presence of neutrons in the ^{13}C pocket and in the TPs via neutron captures on ^{22}Ne (Goriely & Mowlavi 2000; Cristallo et al. 2009; Bisterzo et al. 2011; Lugaro et al. 2012). As a consequence both the mixing profile itself and its effect on the intershell abundance of ^{22}Ne play a significant role. Interestingly, the $-2m$ and $-3m$ cases produce the highest [Pb/Ba] and the lowest [Na/Ba] of all models. However, even the lowest value we find (-0.90) is still higher than the observations (down to -2 dex). Cavanna et al. (2015) reported a revised value of the $^{22}\text{Ne}(p,\gamma)^{23}\text{Na}$ rate measured underground, however, at the temperature of interest (< 20 MK) the new rate is the same as the rate we have used here (Iliadis et al. 2010). On the other hand, the rate of the destruction reaction $^{23}\text{Na}(p,\alpha)^{20}\text{Ne}$ is poorly known (Iliadis et al. 2010). While the issue of the nuclear physics input is still open and needs further investigation, observation of an anticorrelation between the Pb and the Na abundance in CEMP stars may strengthen the possibility that the Pb and Na variations are indeed due to variations in the mixing profile of the PMZ.

5.1 Comparison with meteoritic stardust data

Stardust grains have been recovered from meteorites for the past three decades, and have been used to constrain models of nucleosynthesis processes in the stars from where they originated (Zinner 2014). The vast majority of these grains formed in the expanding envelopes of AGB stars, in particular, silicon carbide (SiC) grains formed in C-rich AGB stars, since $\text{C} > \text{O}$ is a necessary condition for the formation of SiC molecules. They carry a strong signature of s -process nucleosynthesis in the isotopic composition of elements heavier than Fe that are present in trace amounts. Because such compositions can be measured to very high precision, particularly when using the Resonant Ionisation Mass Spectrometry (RIMS) technique (e.g. Liu et al. 2014a,b, 2015), stardust SiC grains provide excellent constraints for stellar models of the s process. On the other hand, we do not know *a priori* the initial mass and metallicity of the parent star of each grain. The general constraints, also coming from the composition of the light elements C, N, Ne, and Si, are that the SiC parent stars should be of metallicity roughly around solar, and should have initial masses below roughly $5 M_{\odot}$ (Lugaro et al. 1999, 2003b).

In Fig. 8 we compare a selection of our models with the composition of the grains. We choose isotopic ratios that are sensitive to the neutron exposure, hence to the features of the ^{13}C pocket, as well as the mass and metallicity of the star. As noted above for the elemental ratios, also in

terms of the isotopic ratios, typically varying the mixing profile produces very similar results as varying its extent in mass, except for the $-3m$ case. Only for the $3 M_{\odot}$, $Z = 0.02$ there are significant differences, where the variations in the mixing profile produces a larger variety of isotopic compositions than variations in M_{PMZ} .

The $^{88}\text{Sr}/^{86}\text{Sr}$ ratio is an excellent tracer of the neutron exposure. It is clear from Fig. 8 that the grains require a neutron exposure lower than that produced using the majority of the mixing profiles and stellar models tested here. There are several ways to achieve this: one is to use the $-3m$ mixing profile, which as discussed above stands out from the others for producing a markedly lower neutron exposure. Another possibility is to increase the stellar metallicity, i.e., when comparing the $3 M_{\odot}$, $Z = 0.01$ to the $3 M_{\odot}$, $Z = 0.02$ model, it is clear that the latter provides a better match to the grains, also for the $m^{1/2}$ and $m^{1/3}$ mixing profiles. In fact, Lugaro et al. (2017) demonstrated that AGB stars of metallicity around $Z = 0.03$, i.e., roughly twice higher than solar, produce most of the signatures observed in the grains for Sr, Zr, and Ba.

In terms of the Zr isotopic ratios, similar conclusions can be drawn: the majority of the models with metallicity lower than solar ($Z = 0.01$) can only match the lowest $^{92}\text{Zr}/^{94}\text{Zr}$ ratio observed in the grains. Lower neutron exposures are required to reach the observed average, i.e., again either using the $-3m$ case, or a higher stellar metallicity. However, only the specific case of the $-3m$ profile in the $1.8 M_{\odot}$, $Z = 0.01$ can reach $^{92}\text{Zr}/^{94}\text{Zr}$ ratios around solar together with $^{96}\text{Zr}/^{94}\text{Zr}$ ratios roughly 50% lower than solar, as measured in many grains.

6 CONCLUSIONS

We have found that varying the mixing profile of the PMZ generally produces the same results as varying the extent of the PMZ. This means that in the vast majority of s -process producing AGB stars, those where ^{13}C burns radiatively:

- (i) the mixing profile and the extent of the PMZ can be considered as the same free parameter, unless the profile is changed to the extreme extent of case $-3m$;
- (ii) when the stellar mass is above $\sim 2 M_{\odot}$, the changes are dominated by the feedback of the mixing profile on the operation of the ^{22}Ne neutron source, rather than of the ^{13}C neutron source itself;
- (iii) the overall effect on the relative s -process distribution is of the order of a factor of two, comparable to typical spectroscopic observational error bars;
- (iv) the Sr, Zr, and Ba composition observed in stardust SiC grains requires lower neutron exposures than those experienced in the majority of our models, the $-3m$ profile is the most promising case, although it cannot match simultaneously all the different ratios.

The low-metallicity AGB model is an exception, where the [Pb/Ba] ratio is significantly affected, with the possible interesting consequences for the Pb abundance in CEMP stars discussed above. For all the other cases, the abundance of ^{12}C in the intershell, which is potentially enhanced by overshoot into the core, the presence of ^{13}C ingestions, which are also affected by the uncertain rate of the $^{13}\text{C}(\alpha,n)^{16}\text{O}$

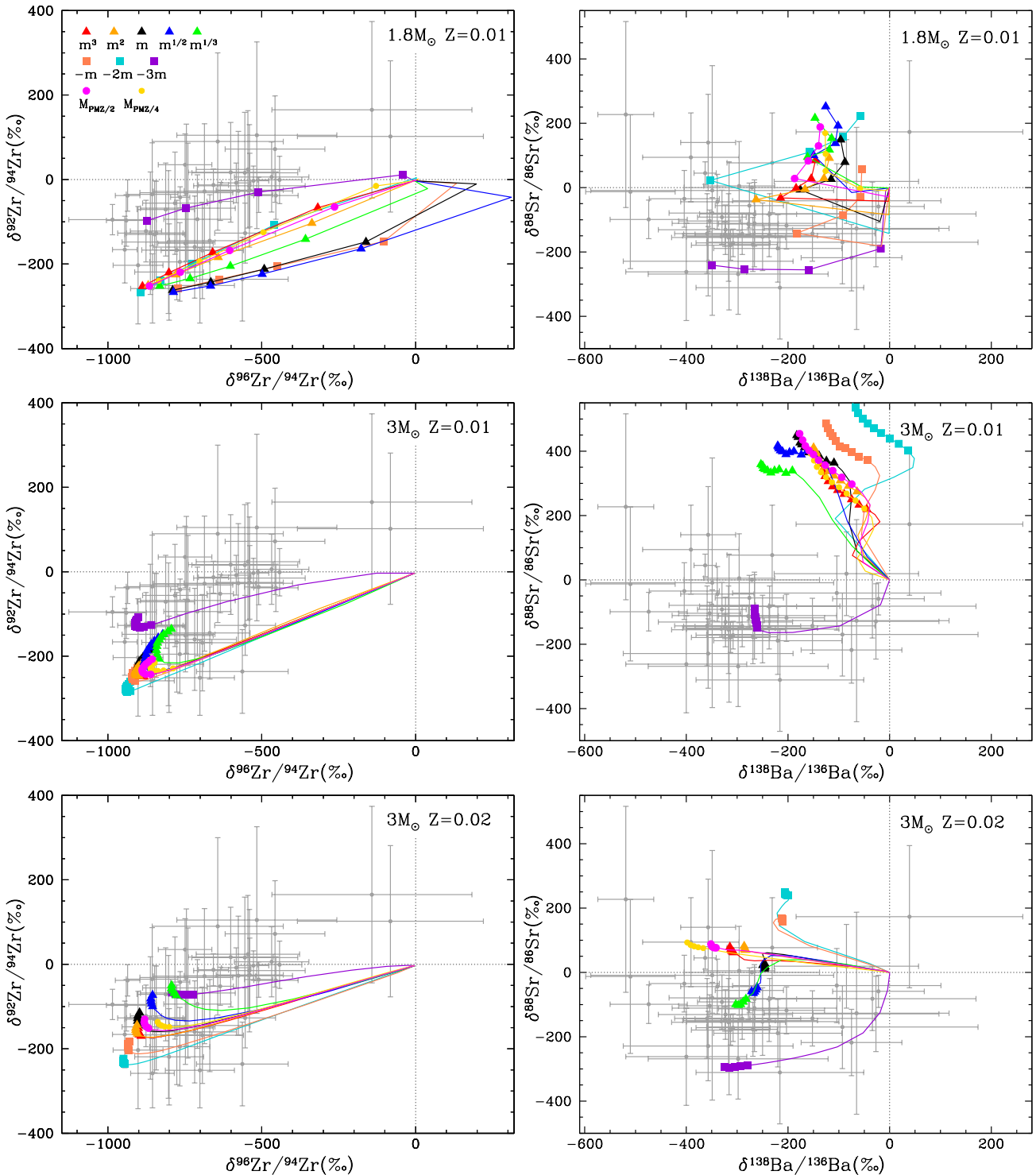


Figure 8. A selection of our models of close to solar metallicity for all the different mixing profile cases is compared to the s -process composition observed in stardust SiC grains from AGB stars (grey symbols with 2σ error bars). We use the standard δ notation, which represent permil variations of the indicated isotopic ratio with respect to the solar value (with $\delta = 0$, by definition). The colored lines show the evolution at the stellar surface starting from the solar initial ratios. The overplotted solid symbols correspond to TDU episodes with a C-rich envelope, the necessary condition for the formation of SiC. The triangles correspond to Set 1 and the squares to Set 2, with the same colors as in all the previous plots. The circles represent the cases where M_{PMZ} was decreased as indicated.

reaction (Guo et al. 2012), and the effect of rotational mixing appear to represent more significant uncertainties for the *s* process than the details of the mixing function leading to the formation of the PMZ. To match the composition of the stardust SiC grains further potential effects due to their parent stars being of different masses and metallicity than considered here need to be taken into account (Lugaro et al. 2017).

7 ACKNOWLEDGMENTS

We thank the anonymous referee for important comments, particularly for pushing us to include Section 5.1 on the comparison with stardust grains. M. L. is a Momentum (“Lendület-2014” Programme) project leader of the Hungarian Academy of Sciences. This research was supported under the Go8-DAAD Australia/Germany Joint research cooperation scheme. R. J. S. is the recipient of a Sofja Kovalevskaja Award from the Alexander von Humboldt Foundation.

REFERENCES

- Abia C., Busso M., Gallino R., Domínguez I., Straniero O., Isern J., 2001, *ApJ*, 559, 1117
- Abia C., Domínguez I., Gallino R., Busso M., Maserà S., Straniero O., de Laverny P., Plez B., Isern J., 2002, *ApJ*, 579, 817
- Asplund M., Grevesse N., Sauval A. J., Scott P., 2009, *ARA&A*, 47, 481
- Battino U., Pignatari M., Ritter C., Herwig F., Denisenkov P., Den Hartogh J. W., Trappitsch R., Hirschi R., Freytag B., Thielemann F., Paxton B., 2016, *ApJ*, 827, 30
- Bazan G., Lattanzio J. C., 1993, *ApJ*, 409, 762
- Bisterzo S., Gallino R., Straniero O., Cristallo S., Käppeler F., 2010, *MNRAS*, 404, 1529
- Bisterzo S., Gallino R., Straniero O., Cristallo S., Käppeler F., 2011, *MNRAS*, 418, 284
- Bisterzo S., Gallino R., Straniero O., Cristallo S., Käppeler F., 2012, *MNRAS*, 422, 849
- Burbidge E. M., Burbidge G. R., Fowler W. A., Hoyle F., 1957, *Rev. Mod. Phys.*, 29, 547
- Busso M., Gallino R., Lambert D. L., Travaglio C., Smith V. V., 2001, *ApJ*, 557, 802
- Busso M., Gallino R., Wasserburg G. J., 1999, *ARA&A*, 37, 239
- Busso M., Lambert D. L., Beglio L., Gallino R., Raiteri C. M., Smith V. V., 1995, *ApJ*, 446, 775
- Cannon R. C., 1993, *MNRAS*, 263, 817
- Cavanna F., Depalo R., Aliotta M., Anders M., Bemmerer D. e. a., 2015, *Physical Review Letters*, 115, 252501
- Cristallo S., Abia C., Straniero O., Piersanti L., 2015, *ApJ*, 801, 53
- Cristallo S., Piersanti L., Straniero O., Gallino R., Domínguez I., Abia C., Di Rico G., Quintini M., Bisterzo S., 2011, *Astrophys. J., Suppl. Ser.*, 197, 17
- Cristallo S., Straniero O., Gallino R., Piersanti L., Domínguez I., Lederer M. T., 2009, *ApJ*, 696, 797
- Cristallo S., Straniero O., Piersanti L., Gobrecht D., 2015, *Astrophys. J., Suppl. Ser.*, 219, 40
- Cybur R. H., Amthor A. M., Ferguson R., Meisel Z., Smith K., Warren S., Heger A., Hoffman R. D., Rauscher T., Sakharuk A., Schatz H., Thielemann F. K., Wiescher M., 2010, *Astrophys. J., Suppl. Ser.*, 189, 240
- Denissenkov P. A., Tout C. A., 2003, *MNRAS*, 340, 722
- Dillmann I., Heil M., Käppeler F., Plag R., Rauscher T., Thielemann F.-K., 2006, in Woehr A., Aprahamian A., eds, *Capture Gamma-Ray Spectroscopy and Related Topics Vol. 819 of American Institute of Physics Conference Series*, KADoNiS- The Karlsruhe Astrophysical Database of Nucleosynthesis in Stars. pp 123–127
- Fishlock C. K., Karakas A. I., Lugaro M., Yong D., 2014, *ApJ*, 797, 44
- Gallino R., Arlandini C., Busso M., Lugaro M., Travaglio C., Straniero O., Chieffi A., Limongi M., 1998, *ApJ*, 497, 388
- García-Hernández D. A., Zamora O., Yagüe A., Utten-thaler S., Karakas A. I., Lugaro M., Ventura P., Lambert D. L., 2013, *A&A*, 555, L3
- Goriely S., Mowlavi N., 2000, *A&A*, 362, 599
- Goriely S., Siess L., 2004, *A&A*, 421, L25
- Guo B., Li Z. H., Lugaro M., Buntain J., Pang D. Y., Li Y. J., Su J., Yan S. Q., Bai X. X., Chen Y. S., Fan Q. W., Jin S. J., Karakas A. I., Li E. T., Li Z. C., Lian G., Liu J. C., Liu X., Shi J. R., Shu N. C., Wang B. X., Wang Y. B., Zeng S., Liu W. P., 2012, *ApJ*, 756, 193
- Heil M., Detwiler R., Azuma R. E., Couture A., Daly J., Görres J., Käppeler F., Reifarth R., Tischhauser P., Ugalde C., Wiescher M., 2008, *Phys. Rev. C*, 78, 025803
- Herwig F., 2000, *A&A*, 360, 952
- Herwig F., 2005, *ARA&A*, 43, 435
- Herwig F., Langer N., Lugaro M., 2003, *ApJ*, 593, 1056
- Herwig F., Pignatari M., Woodward P. R., Porter D. H., Rockefeller G., Fryer C. L., Bennett M., Hirschi R., 2011, *ApJ*, 727, 89
- Hollowell D., Iben Jr. I., 1988, *ApJL*, 333, L25
- Iben Jr. I., Renzini A., 1982, *ApJL*, 263, L23
- Iben Jr. I., Truran J. W., 1978, *ApJ*, 220, 980
- Iliadis C., Longland R., Champagne A. E., Coc A., Fitzgerald R., 2010, *Nuclear Physics A*, 841, 31
- Karakas A. I., 2010, *MNRAS*, 403, 1413
- Karakas A. I., Campbell S. W., Stancliffe R. J., 2010, *ApJ*, 713, 374
- Karakas A. I., García-Hernández D. A., Lugaro M., 2012, *ApJ*, 751, 8
- Karakas A. I., Lattanzio J. C., 2014, *PASA*, 31, e030
- Karakas A. I., Lugaro M., 2016, *ApJ*, 825, 26
- Lambert D. L., Smith V. V., Busso M., Gallino R., Straniero O., 1995, *ApJ*, 450, 302
- Langer N., Heger A., Wellstein S., Herwig F., 1999, *A&A*, 346, L37
- Lattanzio J. C., 1986, *ApJ*, 311, 708
- Lau H. H. B., Gil-Pons P., Doherty C., Lattanzio J., 2012, *Astron. Astrophys.*, 542, A1
- Lederer M. T., Aringer B., 2009, *A&A*, 494, 403
- Liu N., Gallino R., Bisterzo S., Davis A. M., Savina M. R., Pellin M. J., 2014b, *ApJ*, 788, 163
- Liu N., Savina M. R., Davis A. M., Gallino R., Straniero O., Gyngard F., Pellin M. J., Willingham D. G., Dauphas N., Pignatari M., Bisterzo S., Cristallo S., Herwig F., 2014a,

- ApJ, 786, 66
- Liu N., Savina M. R., Gallino R., Davis A. M., Bisterzo S., Gyngard F., Käppeler F., Cristallo S., Dauphas N., Pellin M. J., Dillmann I., 2015, ApJ, 803, 12
- Lugaro M., Davis A. M., Gallino R., Pellin M. J., Straniero O., Käppeler F., 2003b, ApJ, 593, 486
- Lugaro M., Herwig F., Lattanzio J. C., Gallino R., Straniero O., 2003a, ApJ, 586, 1305
- Lugaro M., Karakas A. I., Pető M., Plachy E., 2017, Geochim. Cosochim. Acta, accepted
- Lugaro M., Karakas A. I., Stancliffe R. J., Rijs C., 2012, ApJ, 747, 2
- Lugaro M., Zinner E., Gallino R., Amari S., 1999, ApJ, 527, 369
- Nucci M. C., Busso M., 2014, ApJ, 787, 141
- Piersanti L., Cristallo S., Straniero O., 2013, ApJ, 774, 98
- Pignatari M., Gallino R., Heil M., Wiescher M., Käppeler F., Herwig F., Bisterzo S., 2010, ApJ, 710, 1557
- Pignatari M., Herwig F., Hirschi R., Bennett M., Rockefeller G. e. a., 2016, ApJS, 225, 24
- Raiteri C. M., Busso M., Picchio G., Gallino R., Pulone L., 1991, ApJ, 367, 228
- Raut R., Tonchev A. P., Rusev G., Tornow W., Iliadis C., Lugaro M., Buntain J., Goriely S., Kelley J. H., Schwengner R., Banu A., Tsoneva N., 2013, Physical Review Letters, 111, 112501
- Shingles L. J., Doherty C. L., Karakas A. I., Stancliffe R. J., Lattanzio J. C., Lugaro M., 2015, MNRAS, 452, 2804
- Shingles L. J., Karakas A. I., 2013, MNRAS, 431, 2861
- Siess L., Goriely S., Langer N., 2004, A&A, 415, 1089
- Smith V. V., Lambert D. L., 1990, Astrophys. J., Suppl. Ser., 72, 387
- Straniero O., Chieffi A., Limongi M., Busso M., Gallino R., Arlandini C., 1997, ApJ, 478, 332
- Straniero O., Cristallo S., Piersanti L., 2014, ApJ, 785, 77
- Straniero O., Gallino R., Busso M., Chieffi A., Raiteri C. M., Limongi M., Salaris M., 1995, ApJ, 440, L85
- Straniero O., Gallino R., Cristallo S., 2006, Nuclear Physics A, 777, 311
- Travaglio C., Gallino R., Amari S., Zinner E., Woosley S., Lewis R. S., 1999, ApJ, 510, 325
- Travaglio C., Gallino R., Arnone E., Cowan J., Jordan F., Sneden C., 2004, ApJ, 601, 864
- Travaglio C., Gallino R., Busso M., Gratton R., 2001, ApJ, 549, 346
- Trippella O., Busso M., Palmerini S., Maiorca E., Nucci M. C., 2016, ApJ, 818, 125
- Van Eck S., Goriely S., Jorissen A., Plez B., 2003, A&A, 404, 291
- van Raai M. A., Lugaro M., Karakas A. I., García-Hernández D. A., Yong D., 2012, A&A, 540, A44
- Vassiliadis E., Wood P. R., 1993, ApJ, 413, 641
- Wallner A., Bichler M., Buczak K., Dillmann I., Käppeler F., Karakas A., Lederer C., Lugaro M., Mair K., Mengoni A., Schätzel G., Steier P., Trautvetter H. P., 2016, Phys. Rev. C, 93, 045803
- Zinner E., 2014, in Davis A. M., Exec. Eds. Holland H. D., K. T. K., eds, Meteorites and Cosmochemical Processes. Vol. 1 Treatise on Geochemistry, 2nd Ed. Elsevier, Oxford Presolar Grains. pp 181–213